Article

Reanalyzing Jupiter ISO/SWS Data through a More Recent Atmospheric Model

José Ribeiro [1,2], Pedro Machado [1,2,*], Santiago Pérez-Hoyos [3], João A. Dias [1,2] and Patrick Irwin [4]

1   Institute of Astrophysics and Space Sciences, Observatório Astronómico de Lisboa, Ed. Leste, Tapada da Ajuda, 1349-018 Lisbon, Portugal
2   Faculty of Sciences, University of Lisbon, Campo Grande 016, 1749-016 Lisbon, Portugal
3   Escuela de Ingeniería de Bilbao, Universidad del País Vasco-Euskal Herriko Unibertsitatea, 48013 Bilbao, Spain
4   Atmospheric, Oceanic, and Planetary Physics, Clarendon Laboratory, University of Oxford, Parks Road, Oxford OX1 3PU, UK
*   Correspondence: pmmachado@fc.ul.pt

Abstract: The study of isotopic ratios in planetary atmospheres gives an insight into the formation history and evolution of these objects. The more we can constrain these ratios, the better we can understand the history and future of our solar system. To help in this endeavour, we used Infrared Space Observatory Short Wavelength Spectrometer (ISO/SWS) Jupiter observations in the 793–1500 cm^{-1} region together with the Nonlinear Optimal Estimator for MultivariatE Spectral analySIS (NEMESIS) radiative transfer suite to retrieve the temperature–pressure profile and the chemical abundances for various chemical species. We also used the 1500–2499 cm^{-1} region to determine the cloud and aerosol structure of the upper troposphere. We obtained a best-fit simulated spectrum with $\chi^2/N = 0.47$ for the 793–1500 cm^{-1} region and $\chi^2/N = 0.71$ for the 1500–2499 cm^{-1} region. From the retrieved methane abundances, we obtained, within a 1σ uncertainty, a ^{12}C/^{13}C ratio of 84 ± 27 and a D/H ratio of $(3.5 \pm 0.6) \times 10^{-5}$, and these ratios are consistent with other published results from the literature.

Keywords: Jupiter; vertical structure; spectroscopy; radiative transfer

1. Introduction

Jupiter is the largest planet in the solar system, possessing a very dynamic and inhomogeneous atmosphere, making it a very interesting object to study. From studying the composition of the Jovian atmosphere, we can infer what the conditions were during the planet's formation and how much icy or rocky material was aggregated from the surrounding solar nebula. By studying the chemical species that make up the Jovian atmosphere, we can peer into the past of our solar system.

The temperature field, chemical abundances and isotopic ratios of Jupiter have been studied for decades: with Voyager 1 observations, the composition of the troposphere of the North Equatorial Belt was analyzed, and vertical abundance profiles for various chemical species were obtained (Kunde et al., 1982 [1]). The value of D/H of $3.6^{+1.0}_{-1.4} \times 10^{-5}$ was also determined (Kunde et al., 1982 [1]). From the ground, in Arizona, observations with the McMath–Pierce 60-inch (1.5 m) telescope determined the ^{12}C/^{13}C ratio of Jupiter (91^{+26}_{-13}) (Sada et al., 1996 [2]), and the temperature profile was also determined (Sada et al., 1998 [3]). Results from the Galileo probe mass spectrometer were published by Niemann et al. in 1998 [4], obtaining a ^{13}C/^{12}C ratio of 0.0108 ± 0.0005 (^{12}C/^{13}C = 93 ± 4), corroborating the previous results from Sada et al. [2]. With the Infrared Space Observatory's Short Wavelength Spectrometer (ISO/SWS) instrument, Fouchet et al. [5] derived the volume mixing ratios (q) of ethane at two independent pressure levels for the 12–16 µm range of the Jovian spectrum. They obtained q = $1.0 \pm 0.2 \times 10^{-5}$ at 1 mbar and q = $2.6^{+0.5}_{-0.6} \times 10^{-6}$ at 10 mbar.

On the modeling side, Parkinson et al. [6] offered an alternative interpretation of past determinations of CH_3D. Through modeling and some parameterizations, they studied the effects on the retrieved abundance profile of CH_3D on a standard reference atmosphere and how it affected the D/H ratio in order to explain discrepancies in past D/H determinations through methane, linking past observations with dynamical processes. Fletcher et al. [7] performed a midinfrared mapping of Jupiter's temperatures, aerosol opacity and distribution of chemical species using the Infrared Telescope Facility's Texas Echelon Cross Echelle Spectrograph (IRTF/TEXES), creating 2D maps of upper tropospheric aerosols, phosphine and ammonia, as well as 2D maps of stratospheric ethane and acetylene; they also found an increase in the zonal-average temperature of the Equatorial Belt near the 1–2 mbar level when compared with Cassini Composite Infrared Spectrometer (CIRS) observations from December 2000. Pierel et al. [8] estimated the D/H ratio of Jupiter ($2.95 \pm 0.55 \times 10^{-5}$) by using Cassini CIRS observations, and their results are in agreement with the previous ratio measurements by ISO/SWS by Lellouch et al. [9] of $2.25 \pm 0.35 \times 10^{-5}$. In the UV part of the Jupiter spectrum, Melin et al. [10] analyzed Cassini Ultraviolet Imaging Spectrograph (UVIS) observations of the disk of Jupiter during the 2000–2001 flyby to determine a vertical acetylene abundance profile that is consistent with both CIRS and UVIS. Lastly, they performed a sensitivity study for the Jupiter Icy Moons Explorer (JUICE) ultraviolet spectrograph for the retrieval of ammonia and phosphine abundances, in addition to acetylene and ethane.

However, back in the 1990s, the ISO space telescope was a stepping stone in our understanding of the chemistry and structure of the Jovian atmosphere. The main highlights were the detection of the ν_1 NH_3 band for the first time, the first detection of the ν_3 CH_4 band at 3.3 µm, the detection of water vapor and carbon dioxide in the stratosphere of Jupiter and the determination of the D/H ($1.8^{+1.1}_{-0.5} \times 10^{-5}$, by Lellouch et al. [11]) ratio from the detection of HD rotational lines [12] and from the CH_4 ν_4 band at 7.7 µm and the CH3D ν_6 band at 8.6 µm (CH_3D/CH_4) [9]. It stayed in operation from February 1996 to the depletion of the liquid helium reservoir in April 1998, maintaining limited operations through May of that year.

The ISO/SWS observations continue to be a relevant data set used to obtain new results using more up-to-date atmosphere modeling techniques and line transition databases, such as in the case of the determination of the CH_4 abundance in Jupiter's upper atmosphere by Sánchez-López et al. [13] by modeling the radiance at 3.3 µm, measured by ISO/SWS. The ISO/SWS observations also cover the 5–7 µm (2000–1400 cm^{-1}) window, where methane absorptions/emissions are significant. Cassini's CIRS only went as low as 7.16 µm [14] and Junos's Jovian Infrared Auroral Mapper (JIRAM) only goes up to 5 µm [15], leaving this gap in the spectrum of Jupiter open. Even though IRTF's TEXES can observe this spectral window [16], ISO/SWS has been, so far, the only space facility to have given access to the full midinfrared spectrum of Jupiter. It is also important to highlight that, since the time of the observations, there have been advancements in atmospheric modeling, so it is important to see how more up-to-date atmospheric models impact previous analyses. For these reasons, we argue that ISO/SWS observations are still relevant to this day.

With this study, we aim to constrain the temperature–pressure profile of Jupiter, retrieve the chemical abundance for various chemical species in the Jovian atmosphere and derive the $^{12}C/^{13}C$ and D/H isotopic ratios from the abundance of methane isotopologues, as well as retrieve the aerosol density profiles. Our results are also compared and discussed in the context of previous studies.

2. Observations

The Jupiter ISO/SWS spectrum used in this study, shown in Figure 1, was recorded on 12 April 1996 by the ISO's SWS [17,18] instrument, with the aperture ($14'' \times 20''$ below 12 µm, $14'' \times 27''$ above) centered on the planetary disk, with the long axis aligned perpendicular to the ecliptic, roughly aligned with the central meridian (polar angle = 352°) (Figure 2). The exposure time was 110 min [19], covering planetographic latitudes in the range of

approximately $\pm 33°$ and longitudes in the range of approximately $\pm 22°$ from the central meridian [20]. More details about the reduction, calibration and uncertainties are given in [12,18]. The absolute flux accuracy is about 20% [18,19] and, for this reason, this is the relative error assumed for the observations in this work unless the error is smaller than 300 Jy (0.668 nW cm^{-2} sr^{-1} cm), then we assume it to be 300 Jy. This error limit was provided to us by Dr. Thérèse Encrenaz (private communication). The grating spectrum was convolved to a resolving power of 1500 over the whole spectral range of ISO's SWS [19].
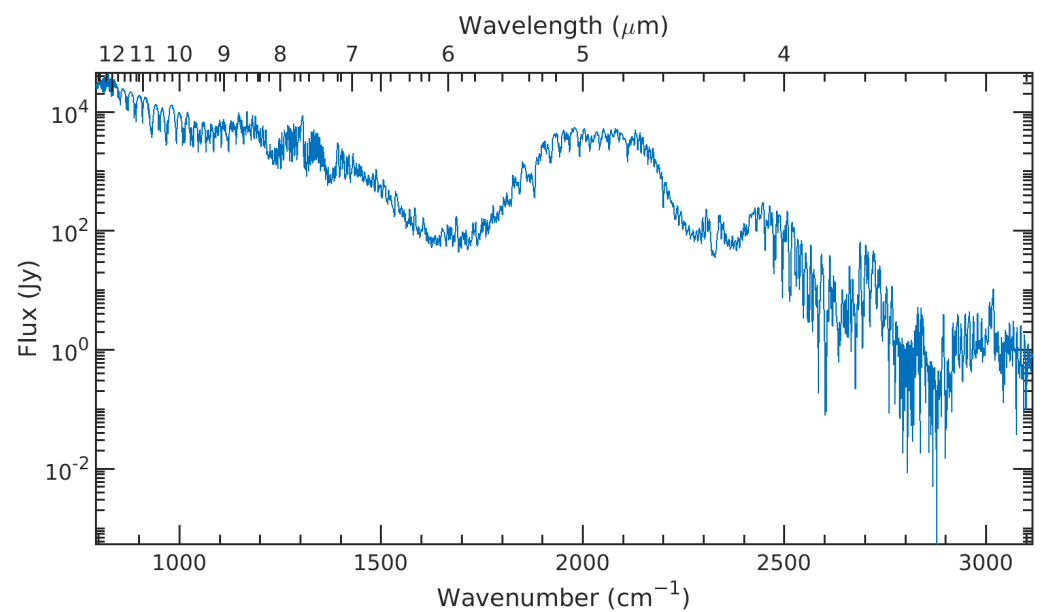

Figure 1. FullISO/SWS Jupiter spectrum referenced in this work.
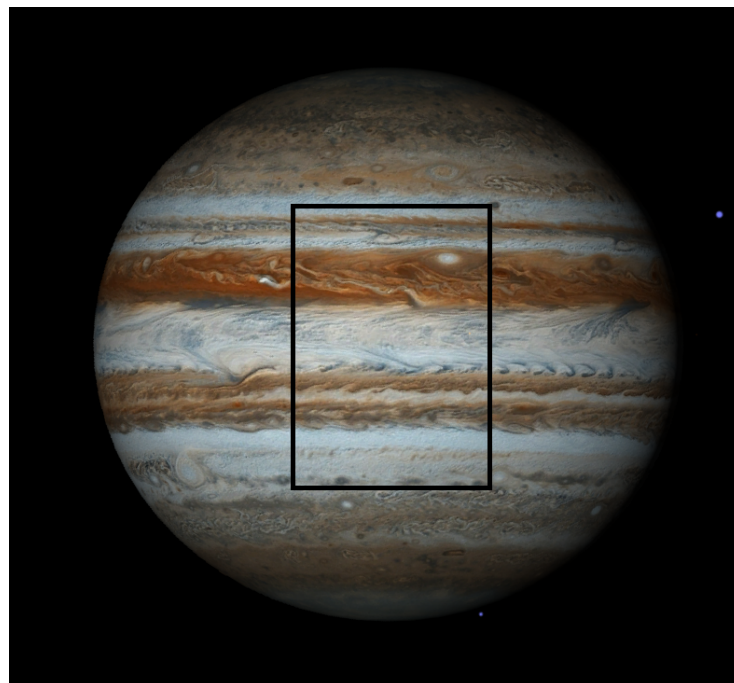

Figure 2. Artistic representation of the ISO/SWS field of view (FOV) (black rectangle) over Jupiter. Jupiter image from StarryNight software(Version: Pro Plus 8; Manufacture: Simulation Curriculum Corp.; Minnetonka, Minnesota, United States of America) with the expected configuration at the time of the observations.

3. Methodology

For this work, we focus on two spectral regions of observation, the 793–1500 cm^{-1} (6.7–12.6 µm) region, where molecular absorptions/emissions play an important role in the features of the spectrum, and the 1500–2499 cm^{-1} (4.0–6.7 µm) region, where aerosols play a more important role. The observation was interpolated to have a spectral resolution of 1 cm^{-1}. The remainder of the spectral range (2500–4000 cm^{-1}) of the observations was not considered for this work, since the spectral line database used was found to be incomplete for wavelengths smaller than 4 microns. Once the database becomes more comprehensive, an analysis of the 2500–4000 cm^{-1} region will be performed in future studies.

3.1. NEMESIS Radiative Transfer Suite

To perform our atmospheric analysis, we used the NEMESIS (Nonlinear Optimal Estimator for MultivariatE Spectral analySIS) radiative transfer suite (Irwin et al., 2008 [21]). This tool allows coverage of both reflection and emission from any planetary atmosphere in our solar system and beyond, from visible to microwave, in scattering and nonscattering environments. The code utilizes an optimal estimator method (Rodgers, 2000) [22] to find the best plausible values of the parameters that define the atmospheric model, with an a priori parameterization of the atmosphere and the observational uncertainties as the starting point.

For this work, we assume nonscattering for the 793–1500 cm^{-1} range, since thermal emission is the predominant effect and aerosols have little to no effect in this spectral range. We assume single scattering in the 1500–2499 cm^{-1} range, since aerosols play a significant role at the 5-micron (2000 cm^{-1}) window.

3.2. Model Atmosphere

For the 793–1500 cm^{-1} region, the model atmosphere used in this work consists of NH_3 (ammonia), PH_3 (phosphine), C_2H_2 (acetylene), C_2H_4 (ethylene), C_2H_6 (ethane), C_4H_2 (diacetylene), He (helium), H_2 (hydrogen gas), $^{12}CH_4$ (methane-12C), $^{13}CH_4$ (methane-13C) and $^{12}CH_3D$ (deuteriomethane 1). The molecular profiles used in this work are from Irwin et al. [23], with the vertical chemical abundance profiles shown in Figure 3.
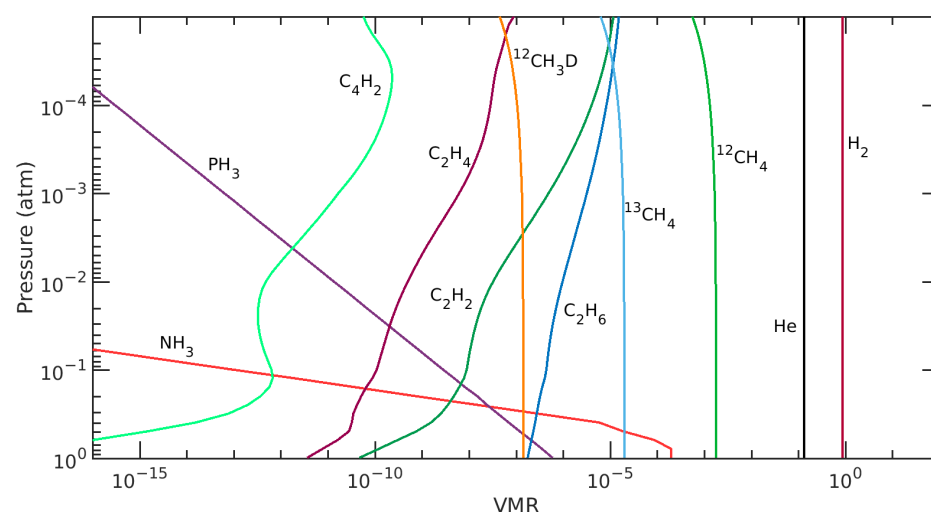

Figure 3. Plot of all the a priori chemical profiles that make up the model atmosphere for the 793–1500 cm^{-1} region.

The a priori temperature profile used is from Sada et al. [3], assuming a 5% a priori uncertainty. The profile is shown in Figure 4. For the 1500–2499 cm^{-1} region, the temperature profile used is the one retrieved from the smaller wavenumber region, adiabatically extrapolated downwards to 10 atm.
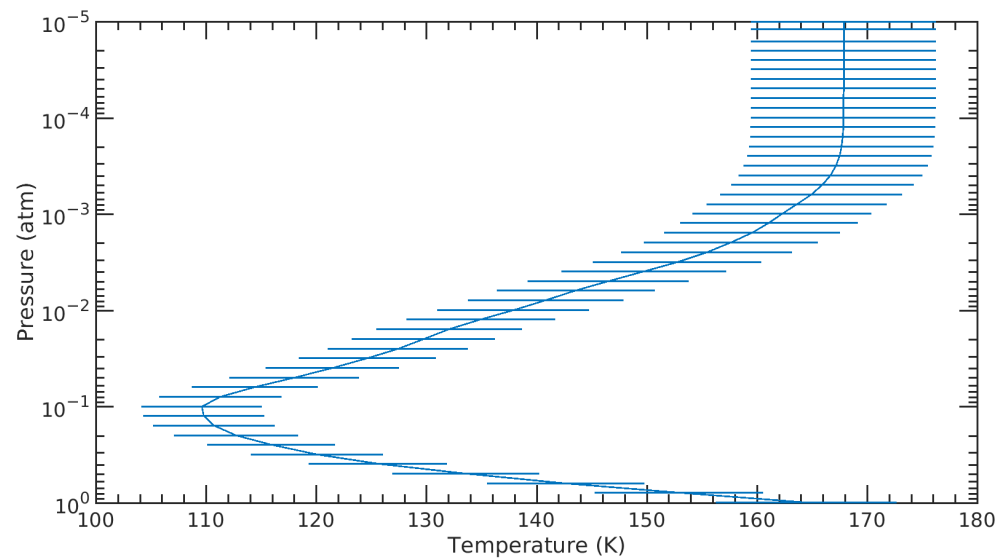
Figure 4. Plot of the a priori temperature profile from Sada et. al., 1998 [3] assuming a 5% a priori uncertainty used in this work.

The k-tables for the absorbing species (NH_3, PH_3, C_2H_6, $^{12}CH_4$, $^{13}CH_4$ and $^{12}CH_3D$) used in this work were generated from the spectral line database from Fletcher et al. [24].

We simultaneously performed a temperature retrieval for 51 atmospheric levels and a simple scaling retrieval for NH_3, PH_3, C_2H_6, $^{13}CH_4$ and $^{12}CH_3D$ for a spectrum with 708 distinct wavenumber values (793–1500 cm^{-1} with a spectral resolution of 1 cm^{-1}). This, in total, translates to a retrieval with 56 free parameters.

To take into account the field of view of ISO/SWS over Jupiter that produced the observed spectrum, we considered 9 points made from the combination of latitude and longitude pairs ranging from +33°, +0° and −33° latitude and +22°, +0° and −22° longitude from the center of the field of view at −2.1° latitude and 352° longitude, assuming equal detector efficiency over the whole field of view. However, the choice of sampling points does not significantly alter the retrieved modeled spectrum. From our initial analysis, the choice of sampling points can be performed in other configurations with no significant changes in the retrieved parameters and model spectrum.

For the 1500–2499 cm^{-1} region, the model atmosphere consists of the same molecules as the 793–1500 cm^{-1} region, using the profiles of the molecules that were previously retrieved. In this range, we also included an H_2O (water) profile from Irwin et al. [25] and a constant abundance GeH_4 (germane) profile from Kunde et al. [1], with the k-tables generated from the spectral line database from Fletcher et al. [24] as well.

Regarding the aerosol properties, two aerosol types were considered as part of the atmospheric model. Based on a preliminary analysis, we assumed the first type to be water (West et al., 2004 [26]) due to the altitude level it is located at, with refractive indices from Hale and Querry [27], and an assumed gamma particle size distribution with a mean particle radius of 10 microns and relative width of 0.1. The other was of ammonia ice with refractive indices from Martonchik et al. [28], and an assumed gamma particle size distribution with a mean particle radius of 10 microns and relative width of 0.1 as well. The fractional cloud cover for both aerosols was considered to be 100% for the whole pressure range, with the a priori cloud profiles shown in Figure 5. The parameters of the water ice cloud are fixed, and they are as such so that the initial forward model spectrum could be as close as possible to the observations. Only the ammonia ice cloud scaling factor parameters are retrieved from the analysis of the 1500–2499 cm^{-1} spectrum. The composition of both clouds and particle size distributions are fixed as well.
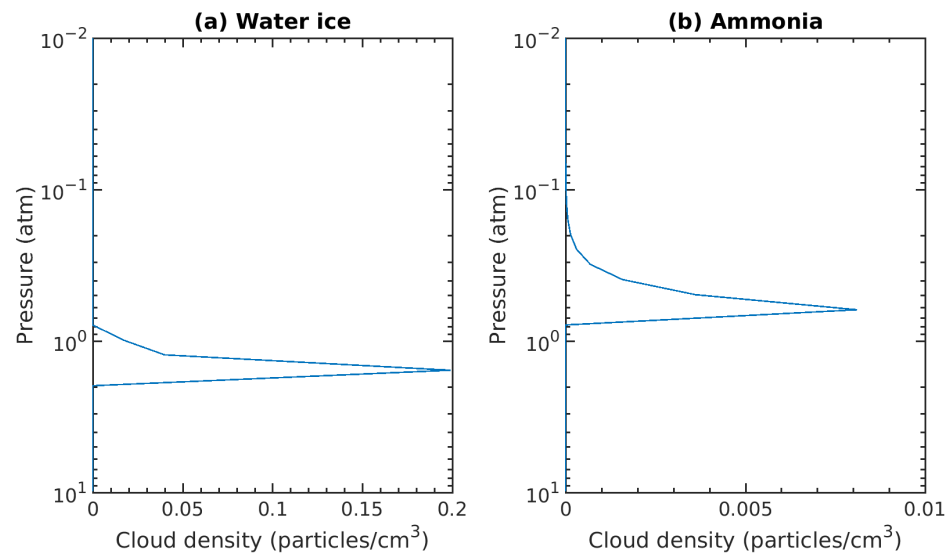
Figure 5. Plot of the a priori cloud density profile for the water ice cloud (**a**). Plot of the a priori cloud density profile for the NH$_3$ cloud (**b**). For pressures beyond the ranges of the plot the density becomes negligible.

We performed the retrieval in single-scattering mode of three parameters of the NH$_3$ cloud: the base height (pressure) from where the pressure is 1 atm (1.01325 $\times$ 10^5 Pa), the base density and the fractional scale height (the ratio of the cloud scale height to the atmospheric scale height, Koukouli et al., 2005 [29]) for 1000 distinct wavenumber values (1500–2499 cm^{-1} with a spectral resolution of 1 cm^{-1}). The cloud base height was fixed for this retrieval.

No FOV averaging was performed for scattering calculations; the retrieval for this region was performed under single-source-point conditions.

4. Results

4.1. Best-Fitting Spectrum

NEMESIS quantifies the goodness of fit using the chi-squared value (χ^2/N):

$$\chi^2/N = \sum \left(\frac{R_{obs} - R_{fit}}{\sigma} \right)^2 / N \tag{1}$$

In Equation (1), N is the total number of distinct wavenumber values that make up the spectrum, R_{obs} is the observed radiance value at a specific wavenumber, R_{fit} is the radiance value of the fit at the same wavenumber and σ is the associated observation error at that same wavenumber.

For the 793–1500 cm^{-1} region, we obtained $\chi^2/N = 0.47$. If we consider, instead, using $N_{free} = N - N_{param}$ ($N_{free} = 708 - 56$), we obtain $\chi^2/N = 0.51$.

Figure 6a shows the simulated spectrum in red and the ISO/SWS Jupiter observation in blue. Plot (b) shows the radiance difference between the observation and the simulated spectrum (observed–simulated), with the error mostly coinciding with the horizontal lines around 1400 cm^{-1}. The differences between the simulated spectrum and the observations are mostly within the error limits. The largest difference, which also surpasses the error at that frequency, is near 800 cm^{-1}. This, however, does not translate into an overly large χ^2 value, since the absolute values of radiance are large as well. We start to see, in plot (c), the largest values of χ^2 beyond 1200 cm^{-1}, with a large value near 1250 cm^{-1}. Since, in this region, we have smaller values of radiance, small deviations from the error limits translate into large values of χ^2. This region of the spectrum is where methane absorptions/emissions start becoming more relevant.
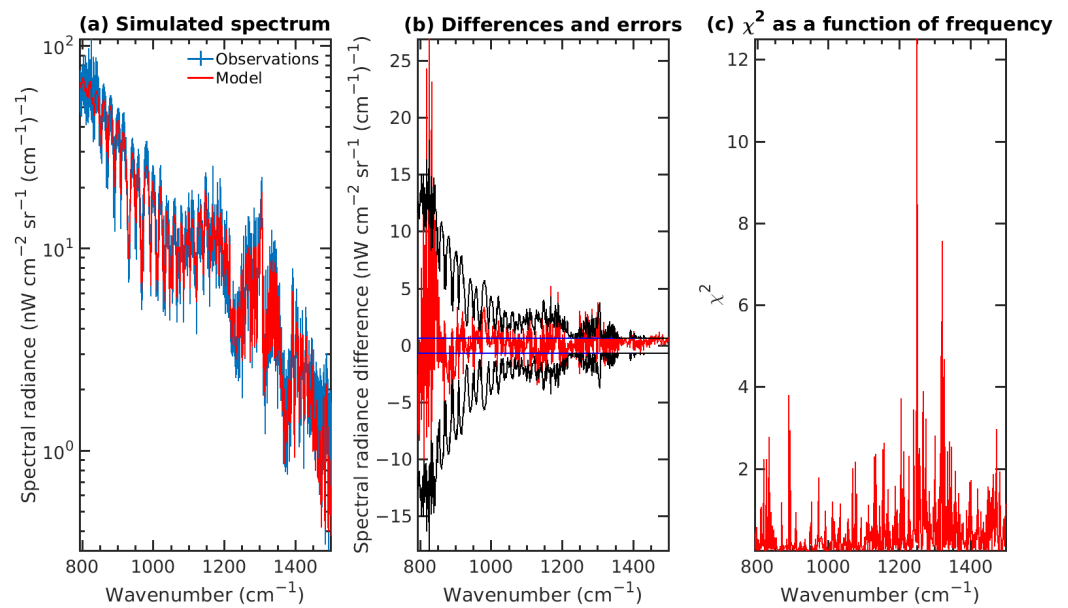
Figure 6. Simulated spectrum for the 793–1500 cm^{-1} region (red) and observed Jupiter spectrum (blue) by ISO-SWS (**a**). Radiance difference between the observation and the simulated spectrum (red), the 300 Jy (0.668 nW cm^{-2} sr^{-1} cm) error limit (blue) and the error of the observations (black) used in this work (**b**). χ^2 as a function of wavenumber (**c**).

As seen in Figure 6c, there is an upward trend in the values of χ^2 with wavenumber, peaking near 1200 cm^{-1}, where methane absorptions/emissions start becoming more relevant.

For the 1500–2499 cm^{-1} region, we obtained $\chi^2/N = 0.71$. If we consider, instead, using $N_{free} = N - N_{param}$ ($N_{free} = 1000 - 3$), we obtain the same value. As seen in Figure 7 (right plot), the largest χ^2 values are around 2000 cm^{-1}, where the effects from aerosols are the most significant.
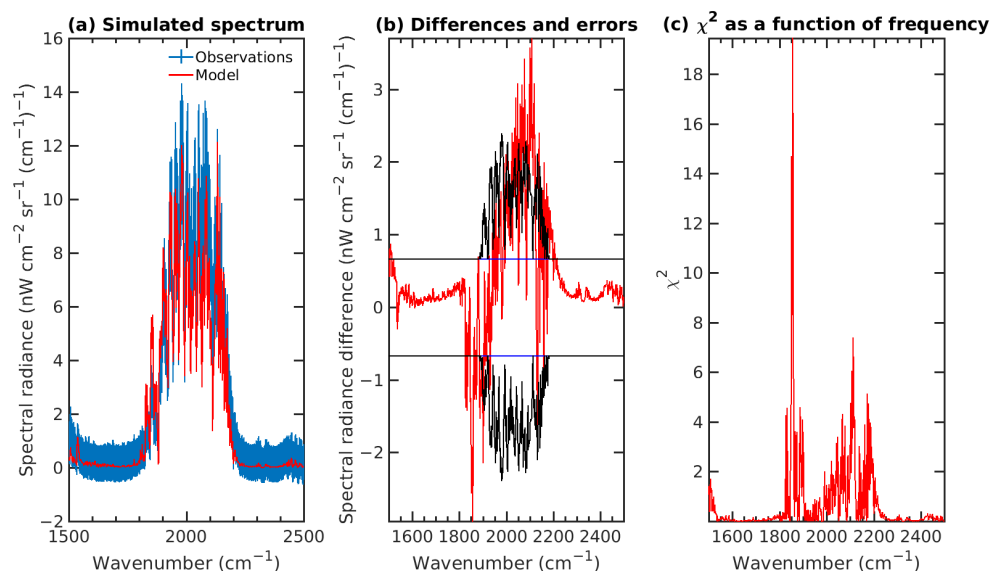

Figure 7. Simulated spectrum for the 1500–2499 cm^{-1} region (red) and observed Jupiter spectrum (blue) by ISO-SWS (**a**). Radiance difference between the observation and the simulated spectrum (red), the 300 Jy (0.668 nW cm^{-2} sr^{-1} cm) error limit and the error of the observations (black) used in this work (**b**). χ^2 as a function of wavenumber (**c**).

Figure 7a shows the simulated spectrum in red and the ISO/SWS Jupiter observation in blue. Plot (b) shows the radiance difference between the observation and the

simulated spectrum (observed–simulated). The deviations from the error limit happen around 2000 cm^{-1}, where the simulated spectrum is brighter for wavenumbers smaller than 2000 cm^{-1} and dimmer for wavenumbers greater than 2000 cm^{-1}. Plot (c) shows the obtained values of χ^2 as a function of frequency, where we see the largest peak in χ^2 near 1850 cm^{-1}.

4.2. Retrieved Parameters

In Figure 8, we show the a priori profiles and our retrieved profiles and compare them with other profiles from various other works for the 793–1500 cm^{-1} region. Plot (a) shows our retrieved NH_3 profile and how it compares with the profiles found in Fletcher et al. [7] and Melin et al. [10]. Our retrieved profile follows the profile from Fletcher et al. [7] from 0.4 to 0.8 atm more closely than the one from Melin et al. [10]. Plot (b) shows our retrieved PH_3 and that it only coincides with the one from Fletcher et al. [7] near 1 atm and 0.3 atm. The profile from Fletcher et al. [7] has a higher "knee" pressure level and a faster decrease in abundance than the one we retrieved. Plot (c) shows our retrieved C_2H_6 profile and that the profile from Fouchet et al. [5] has a higher VMR than the one we retrieved for pressures <0.1 atm and a smaller VMR for pressures >0.1 atm. Plot (d) shows our retrieved $^{13}CH_4$ and $^{12}CH_3D$ profiles. The a priori of $^{12}CH_4$ matches the one from Sada et al. very closely [3]. The $^{13}CH_4$ closely follows the a priori profile, with it being within the error bars. The retrieved $^{12}CH_3D$ profile follows the one from Parkinson et al. [6] more closely than the a priori one for pressures higher than 10^{-3} atm.
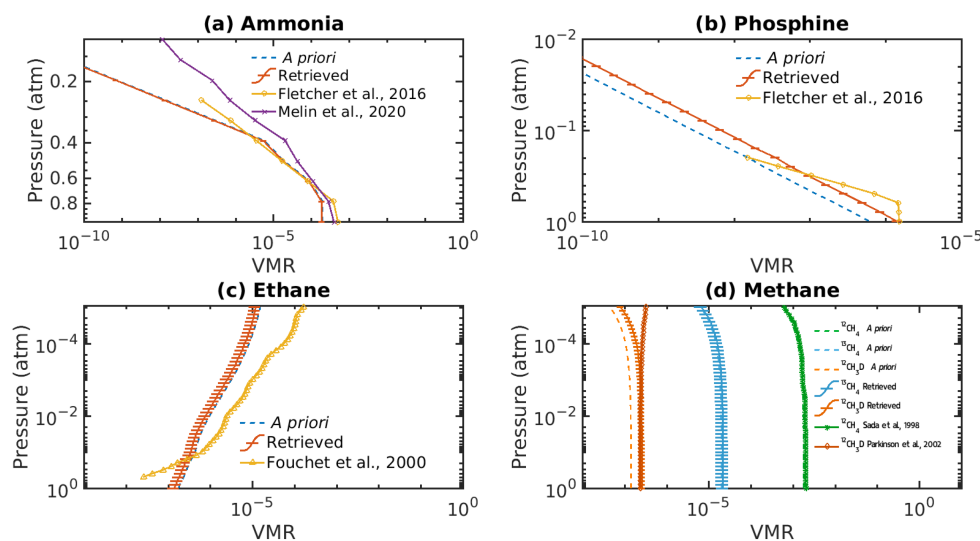

Figure 8. Our retrieved vertical profiles with horizontal error bars of (**a**) ammonia [7,10], (**b**) phosphine [7], (**c**) ethane [5] and (**d**) three methane isotopologues considered for this atmosphere model [3,6] for the 793–1500 cm^{-1} region, as well as the a priori profiles and profiles from various other works.

In Table 1, we show the retrieved scaling factors (the multiplicative factor that is applied to the a priori profile in order to obtain the retrieved profile) and errors for each of the molecules retrieved.

Table 1. Retrieved scaling factors and errors for the simple scaling retrieval of the molecules and corresponding volume mixing ratio (VMR) at 0.4 atm.

Molecule	Scaling Factor	VMR at 0.4 atm
NH_3	0.9 ± 0.2	$5 \pm 1 \times 10^{-6}$
PH_3	2.3 ± 0.3	$1.6 \pm 0.2 \times 10^{-7}$
$^{13}CH_4$	1.1 ± 0.3	$2.2 \pm 0.7 \times 10^{-5}$
$^{12}CH_3D$	1.8 ± 0.3	$2.6 \pm 0.5 \times 10^{-7}$
C_2H_6	0.8 ± 0.2	$2.0 \pm 0.6 \times 10^{-7}$

We show, in Figure 9, our retrieved temperature–pressure profile and compare it with other results from the literature, as well as how the temperature profile changed after the retrieval. Our retrieved profile is colder from 1 to 0.1 atm when compared with the used a priori profile Sada et al. [3], as well as the Fletcher et al. [7] and Melin et al. [10] profiles. From 0.1 to 0.01 atm, the retrieved profile follows the temperature profile from Fletcher et al. more closely [7]. For higher altitudes, the retrieved profile starts to converge towards the a priori profile from Sada et al. [3], with the error bars increasing in size. Our retrieved profile does not show the increase in temperature near 0.01 atm found in the equatorial profile from Melin et al. [10], nor the increase in temperature at 0.001 atm from the various profiles found in Fletcher et al. [7].
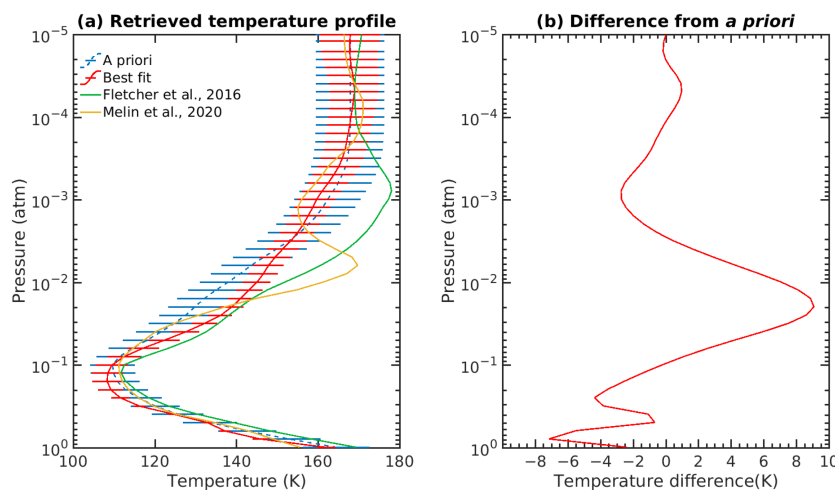

Figure 9. Retrieved pressure–temperature profile for the 793–1500 cm^{-1} region (red), a priori profile (blue) and various profiles from the literature (**a**) [7,10]. Temperature changes (retrieved a priori) after the retrieval as a function of pressure (**b**).

In Figure 10a, we show our retrieved NH_3 cloud density profile for the 1500–2499 cm^{-1} region and how it compares with the a priori cloud density profile. Plot (b) shows the retrieved optical thickness values of the NH_3 cloud as a function of wavenumber, with the values ranging from 1.95 to 2.18. The a priori and retrieved parameter values to model the NH_3 cloud are given in Table 2. The cloud base altitude was fixed at 6 ± 10 km above where the pressure is 1 atm ($0.77 \, ^{+0.38}_{-0.28}$ atm).

Table 2. A priori and retrieved values of the parameters used to model the NH_3 cloud.

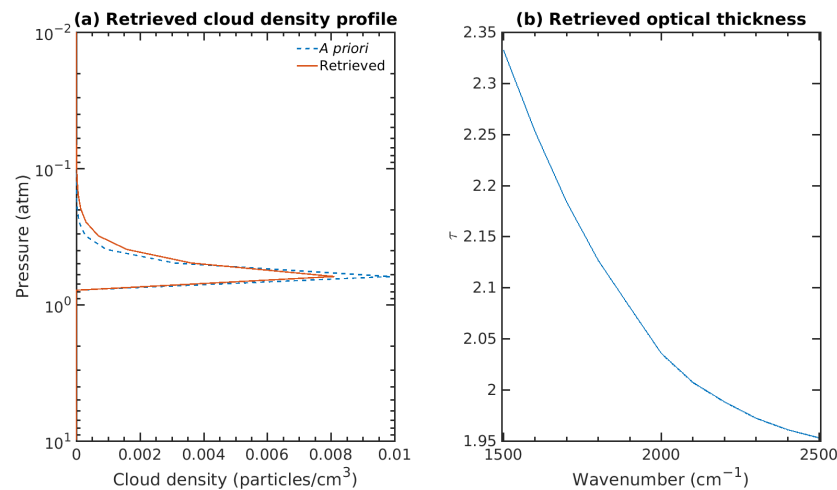| Parameter	A Priori	Retrieved Value
Cloud base density (part/cm^3)	$99 \pm 1 \times 10^{-4}$	$81 \pm 1 \times 10^{-4}$
Fractional scale height	0.2 ± 0.1	0.3 ± 0.1

Figure 10. Retrieved NH_3 cloud density profile for the 1500–2499 cm^{-1} region (**a**). Retrieved optical thickness of the NH_3 cloud as a function of wavenumber (**b**).

4.3. Sensitivity Analysis

We performed a partial differences analysis that consisted of calculating the difference between spectral radiance when the volume mixing ratio of a specific molecule is increased by 5% at a specific altitude/pressure level and the spectral radiance when the volume mixing ratio is decreased by 5% for the same molecule at the same altitude/pressure level. This was performed for every molecule and altitude/pressure level. This allows us to see where in the spectrum we have an increase in absorption or emission and at what altitude/pressure level these occur. The same process was applied to the temperature profile as well, calculating the difference between spectral radiance when the temperature is increased by 5% K at a specific altitude/pressure level and the spectral radiance for when the volume mixing ratio is decreased by 5% K.

Figure 11 shows our partial differences analysis for all the molecules of interest, as well as for temperature. From these, we show that the most intense absorptions/emissions are due to NH_3, PH_3, C_2H_6 and methane. Absorption due to NH_3 and PH_3 occurs from 793 to 1200 cm^{-1} around the 0.4 atm pressure level, with faint absorption from $^{13}CH_4$ near 1200 cm^{-1} and less in the 1400 to 1500 cm^{-1} region and absorption due to $^{12}CH_3D$ present between 1100 and 1200 cm^{-1} below 0.1 atm. From 1200 to 1400 cm^{-1}, we have $^{13}CH_4$ emission from 0.01 to 0.0001 atm, as well as some $^{12}CH_3D$ emission around 1150 cm^{-1}. C_2H_6 absorptions/emissions are limited to the 793 to 900 cm^{-1} region, with absorption happening around 0.3 atm and turning into emission at higher altitudes in the atmosphere. The temperature plot is sensitive to all the absorptions/emissions due to the molecules that make up the model, leading to absorptions/emissions appearing in the plot in the same regions of the wavenumber spectrum and pressure level. An increase in temperature makes these regions appear brighter, regardless of whether there is emission or absorption. These plots show what altitude levels we are sounding for each of the parameters we retrieved and to what part of the spectrum they correspond.

We also determined the improvement factor (Equation (2)) (Irwin et al., 2014 [30]). This allows us to have an idea of how sensitive our fit is to each of the parameters we are retrieving. The closer the value of the improvement factor is to 1, the more significant that parameter is to the retrieval, while the closer it is to 0, the less information we gain from retrieving that parameter. σ_{ret} is the error of a certain parameter, and x is the value of the parameter itself. The *ret* and *apr* correspond to the retrieved and the a priori values:

$$I = 1 - \frac{\sigma_{ret}}{x_{ret}} \frac{x_{apr}}{\sigma_{apr}} \qquad (2)$$

Table 3 shows the calculated improvement factor for each of the molecules that were retrieved. The most significant parameters were the scaling factors of PH_3, NH_3 and $^{12}CH_3D$, while the retrieval was not as sensitive to the retrieval of the $^{13}CH_4$ and C_2H_6 profiles.

In Figure 12, we show our bracketing analysis on the a priori temperature profile. We increased and decreased the original a priori profile from Sada et al. [3] by 10 K and performed retrievals to see if the profile still converged to a similar temperature–pressure profile as the one we obtained. Despite some slight differences, they are within the error bars of each other, with the biggest discrepancies happening near the tropopause and beyond 0.001 atm. The other plot (right) shows the improvement factor for the three profiles, which, once again, are very similar to each other. The hottest profile shows the smallest improvement factor of the three, while the coldest one shows the largest improvement factor until up to 10^{-4} atm, where the coldest profile starts having the worst improvement factor of the three and the hottest profile the best of the three. The important thing to note here is how the improvement factor decreases beyond the 0.02 atm pressure level and when nearing the tropopause. This indicates that we are not sensitive to these pressure levels in particular and are most sensitive to levels around 100 s of mbar.
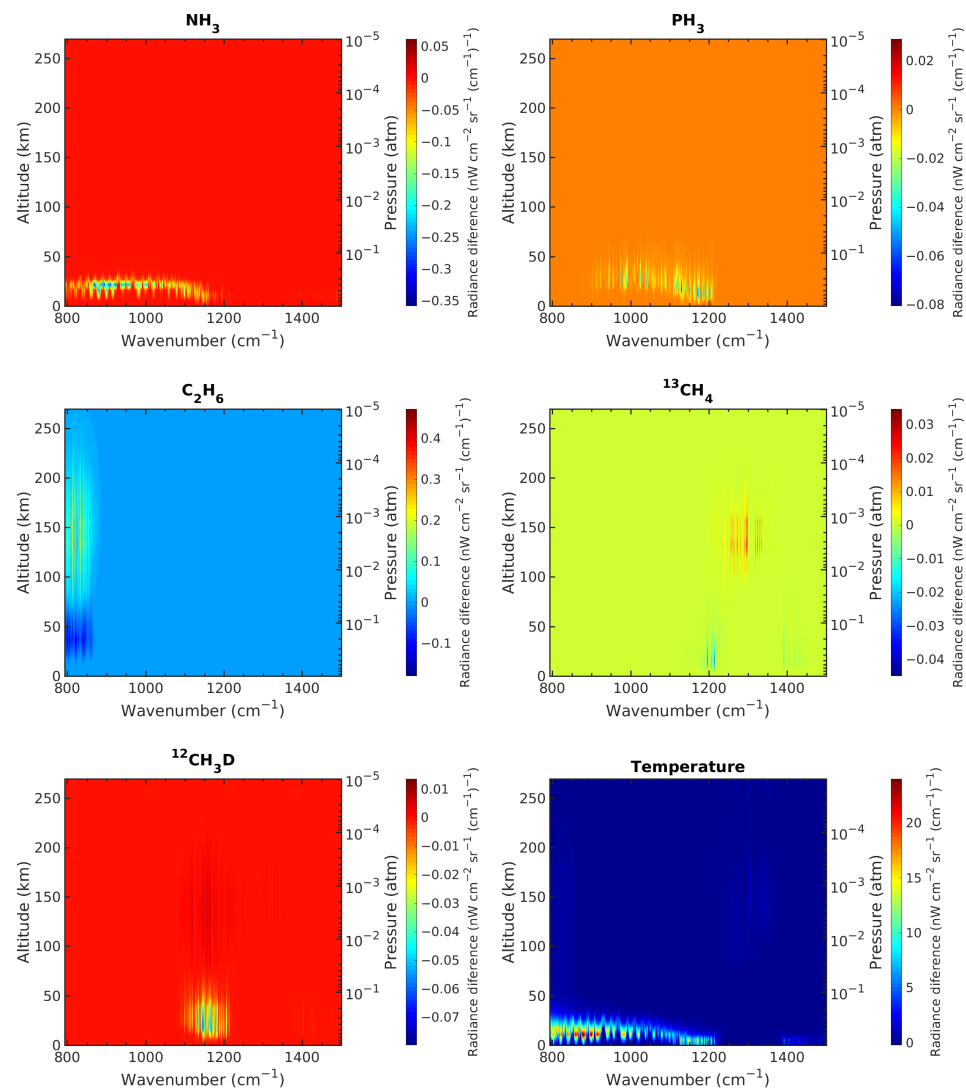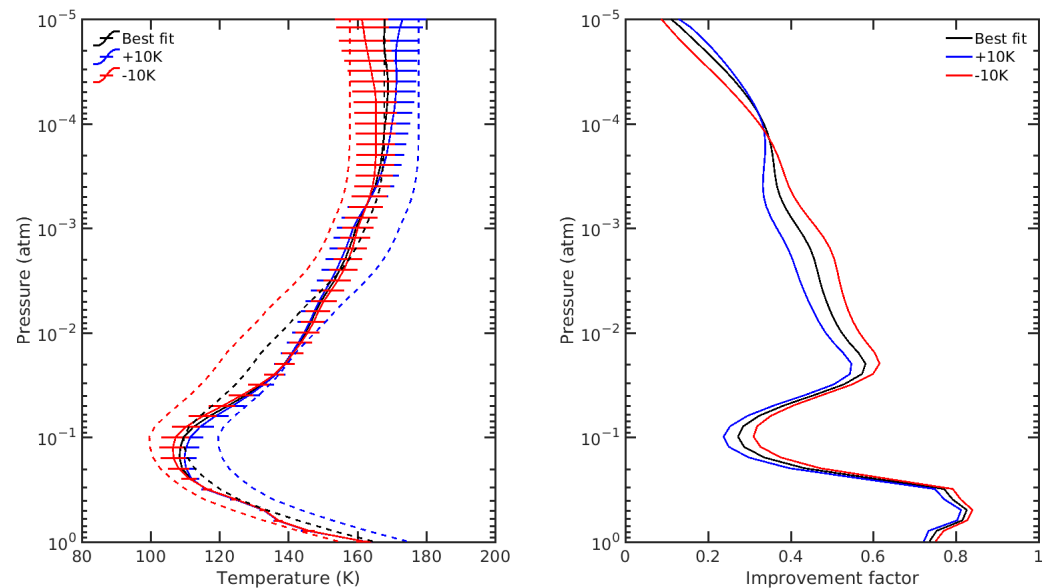

Figure 11. Partial differences analysis plots for NH_3, PH_3, C_2H_6, $^{13}CH_4$, $^{12}CH_3D$ and temperature, showing where in altitude and frequency emission/absorption occurs due to an increase in abundance/temperature.

Table 3. Improvement factor of molecules.

Molecule	Improvement Factor
NH_3	0.65
PH_3	0.73
C_2H_6	0.38
$^{13}CH_4$	0.35
$^{12}CH_3D$	0.64

Figure 12. Bracketing of temperature: Retrieved temperature profiles (continuous) for just a temperature retrieval to test the sensibility of the retrieval to the temperature profile and the a priori temperature profiles (**left**). Improvement factor of temperature profile as a function of pressure (**right**).

5. Discussion

5.1. Temperature

Comparing our results with those from the literature, for pressures higher than 0.1 atm, our retrieved temperature profile appears to be a few degrees colder than what is found in other publications, with slightly colder atmospheric layers below Jupiter's tropopause and a colder tropopause as well. Above the tropopause, the profile starts to converge more closely with the one from Sada et al. [3], leaning more towards the one from Fletcher et al. [7] until about 0.02 atm, where it goes back to converging and following the a priori profile from Sada et al. more closely [3]. We do not see the inversions found in Melin et al. [10], since we are not sensitive to the temperature variation in the equatorial stratosphere due to the observations analyzed in this work covering a larger range of latitudes, thus attenuating the effects of Jupiter's quasi-quadrennial oscillation (QQO) that are clearly seen in the temperature profile from Melin et al. [10] for pressures <10 mbar. The increase in temperature at 0.001 atm found in Fletcher et al. [7] can be seen in the paper itself when they compare their results with the ones from the December 2000 Cassini CIRS 2.5 cm^{-1} observations. In their paper, they show that they measured an increase in temperature of up to 20 K from 1–2 mbar within a $-20°$ to $20°$ planetographic latitude, showing that the Equatorial Zone has had significant changes in temperature over time. Given the time proximity of the ISO/SWS observations with the Cassini CIRS observations when compared with the TEXES observations from Fletcher et al. [7], the difference in temperature near the 1 mbar level is to be expected.

As seen from our sensitivity analysis, the temperature profile is more sensitive for pressure levels below the Jovian tropopause and slightly less for pressure levels above it.

The sensitivity drops significantly at 10^{-3} atm. This translates into a lower accuracy in the retrieval of the temperature near 0.1 atm compared with the previously stated pressure regions. This higher sensitivity in these specific pressure ranges is correlated with where, in altitude, absorption/emission from molecular species occurs in the atmosphere, as seen in Figure 11.

5.2. Chemical Species

Most of the retrieved chemical species have their absorptions/emissions happening at pressures higher than 0.1 atm, with the exception of C_2H_6, where we have emission at pressures lower than 0.1 atm and absorption at higher pressures. Given that the type of retrieval was simple scaling, we are only retrieving a good value for a pressure range, simply fitting the profile in accordance to where in altitude the absorptions/emissions are more intense or significant. This leads to a big difference, which is seen in our retrieved C_2H_6 profile when compared with the one from Fouchet et al. [5] or the NH_3 PH_3 profiles when compared with Melin et al. [10] and Fletcher et al. [7]. However, our retrieved profiles for these specific molecules appear to coincide with the profiles from the literature at the pressure levels where the absorptions/emissions appear to be strongest.

Ideally, one would perform an analogous retrieval to that of temperature for these molecules to see if they follow the ones found in the literature more closely. But this would increase by at least fifty times the number of retrieved variables, leading to degeneracy problems.

Regarding the other molecules that make up the atmospheric model, their abundance is fixed, and the emissions of the most abundant molecules, namely $^{12}CH_4$, H_2 and He, are used as tracers to determine the temperature–pressure profile. During our initial analysis, temperature was the major contributor to the fitting of the model to the observations. Retrieving temperature with any of these three species simultaneously with temperature caused problems in the retrieval, either leading to erroneous or impossible values of VMR or no improvement in the optimal estimator, while producing multiple temperature inversions where there should not be any in the temperature profile. The other molecules had insignificant or no absorption/emissions in this region of the spectrum when we performed our partial differences analysis on them. So, we chose not to perform retrievals of them, with no detriment in the goodness of fit of the obtained simulated spectrum.

5.3. Isotopic Ratios

From the retrieved abundance profiles of methane, we performed the isotopic ratio study for $^{12}C/^{13}C$ following Equation (3) (inverse for $^{13}C/^{12}C$ ratio) and D/H following Equation (4), where VMR correspond to the values of the volume mixing ratio for each molecule at each level. The results of the average across all pressure levels considered in this work are shown in Table 4.

$$^{12}C/^{13}C = \frac{vmr_{^{12}CH_4} + vmr_{^{12}CH_3D}}{vmr_{^{13}CH_4}} \tag{3}$$

$$D/H = \frac{vmr_{^{12}CH_3D}}{3vmr_{^{12}CH_3D} + 4vmr_{^{12}CH_4} + 4vmr_{^{13}CH_4}} \tag{4}$$

We obtained ratios that are within the intervals of the ones found in other published works. Our $^{12}C/^{13}C$ is lower than the one found in Sada et al. [2] and the one found in Niemann et al. [4]. It is also important to note that our errors are larger when compared with the other works, mainly due to the big uncertainty in the retrieved $^{13}CH_4$ profile.

Table 4. Obtained isotopic ratios with 1σ uncertainties and comparison with other results from the literature.

Ratios	Our Results	Other Results	References
$^{12}C/^{13}C$	84 ± 27	91^{+26}_{-13} 93 ± 4 93.5 ± 0.7 (Solar)	Sada et al., 1996 [2] Niemann et al., 1998 [4] Lyons et al., 2018 [31]
D/H	$3.5 \pm 0.6 \times 10^{-5}$	$3.6^{+1.0}_{-1.4} \times 10^{-5}$ $2.95 \pm 0.55 \times 10^{-5}$	Kunde et al., 1982 [1] Pierel et al., 2017 [8]

Regarding the D/H ratio, we obtained a lower value than the one found in Kunde et al. [1], with a smaller error as well; however, the result from Pierel et al. [8] has a lower value for the D/H, as well as a smaller error when compared with the one we obtained, but they are within the error bar interval of each other.

All the errors were computed following the optimal estimator formalism (Rodgers et al.) [22], and the errors in the ratios correspond to a 1σ uncertainty to the expected value.

5.4. Aerosols

Our retrieved results for the NH_3 aerosol cloud are dependent on the a priori deeper and thicker H_2O cloud. This deep cloud was required to be inserted in the model to suppress the overall excess brightness in the spectrum at the 5 µm window. Depending on the initial aerosol density profile of this cloud, the retrieved parameters of the NH_3 would change. As such, we constrained our retrieved parameters for the NH_3 cloud to be near the characteristics found by Fletcher et al. [7], with a cloud base altitude near 0.7 atm and optical depth between 2 and 3.

The optical depth of the water cloud varies from 45 to 38 with frequency, so it can be assumed to be a thick, semi-infinite cloud. What we can say is that where the cloud base is located in altitude is where the suppression of radiance is the strongest. For the same profile shape and density, at higher pressures, the model spectrum is not dimmed as much as it is when the cloud base is located near 2 atm.

6. Conclusions

Despite the circumstances of the observations, we managed to use a more up-to-date radiative transfer model to retrieve various atmospheric characteristics of Jupiter for the 793–1500 cm^{-1} region and the 1500–2499 cm^{-1} region:

- We successfully obtained a simulated spectrum of the atmosphere of Jupiter with $\chi^2/N = 0.47$ for the 793–1500 cm^{-1} region;
- We retrieved a temperature profile that is colder than what is found in other published works for pressures higher than 0.1 atm;
- We retrieved various chemical species, obtaining an increase in abundance for PH_3 and an increase for $^{13}CH_4$ and $^{12}CH_3D$ when compared with the a priori profiles;
- From the methane abundance profiles, we obtained a $^{12}C/^{13}C$ ratio of 84 ± 27 and a D/H ratio of $(3.5 \pm 0.6) \times 10^{-5}$, in good agreement with previous works;
- We successfully obtained a simulated spectrum of the atmosphere of Jupiter with $\chi^2/N = 0.71$ for the 1500–2499 cm^{-1} region;
- We retrieved an aerosol density profile for an NH_3 cloud with a cloud base altitude at 6 ± 10 km and a fractional scale height of 0.3 ± 0.1;

We intend to conduct follow-up work in the future regarding the determination of the $^{15}N/^{14}N$ ratio from NH_3, an improvement of the retrieval of the NH_3, PH_3 and C_2H_6 profiles, and explore the rest of the wavenumber range of these observations (2500–4000 cm^{-1}).

Abbreviations

The following abbreviations are used in this manuscript:

ISO	Infrared Space Observatory
SWS	Short Wavelength Spectrometer
NEMESIS	Non-linear Optimal Estimator for MultivariatE Spectral analySIS
CIRS	Composite Infrared Spectrometer
IRTF	Infrared Telescope Facility
TEXES	Texas Echelon Cross Echelle Spectrograph
JIRAM	Jovian Infrared Auroral Mapper
JUICE	Jupiter Icy Moons Explorer
VMR	Volume Mixing Ratio
FOV	Field of View

References

1. Kunde, V.; Hanel, R.; Maguire, W.; Gautier, D.; Baluteau, J.P.; Marten, A.; Chedin, A.; Husson, N.; Scott, N. The tropospheric gas composition of Jupiter's north equatorial belt /NH3, PH3, CH3D, GeH4, H2O/ and the Jovian D/H isotopic ratio. *Astrophys. J.* **1982**, *263*, 443–467. [CrossRef]
2. Sada, P.V.; McCabe, G.H.; Bjoraker, G.L.; Jennings, D.E.; Reuter, D.C. 13C-Ethane in the Atmospheres of Jupiter and Saturn. *Astrophys. J.* **1996**, *472*, 903. [CrossRef]
3. Sada, P.V.; Bjoraker, G.L.; Jennings, D.E.; McCabe, G.H.; Romani, P.N. Observations of CH_4, C_2H_6, and C_2H_2 in the Stratosphere of Jupiter. *Icarus* **1998**, *136*, 192–201. [CrossRef]
4. Niemann, H.B.; Atreya, S.K.; Carignan, G.R.; Donahue, T.M.; Haberman, J.A.; Harpold, D.N.; Hartle, R.E.; Hunten, D.M.; Kasprzak, W.T.; Mahaffy, P.R.; et al. The composition of the Jovian atmosphere as determined by the Galileo probe mass spectrometer. *J. Geophys. Res. Planets* **1998**, *103*, 22831–22846. [CrossRef] [PubMed]
5. Fouchet, T.; Lellouch, E.; Bézard, B.; Feuchtgruber, H.; Drossart, P.; Encrenaz, T. Jupiter's hydrocarbons observed with ISO-SWS: Vertical profiles of C_2H_6 and C_2H_2, detection of CH_3C_2H. *Astron. Astrophys.* **2000**, *355*, L13–L17. [CrossRef]
6. Parkinson, C.; Jaffel, L.; McConnell, J. Deuterium Abundance from HD and CH3D Reservoirs in the Atmosphere of Jupiter. *Bull. Am. Astron. Soc.* **2001**, *33*, 1042.
7. Fletcher, L.N.; Greathouse, T.K.; Orton, G.S.; Sinclair, J.A.; Giles, R.S.; Irwin, P.G.J.; Encrenaz, T. Mid-infrared mapping of Jupiter's temperatures, aerosol opacity and chemical distributions with IRTF/TEXES. *Icarus* **2016**, *278*, 128–161. [CrossRef]
8. Pierel, J.D.R.; Nixon, C.A.; Lellouch, E.; Fletcher, L.N.; Bjoraker, G.L.; Achterberg, R.K.; Bézard, B.; Hesman, B.E.; Irwin, P.G.J.; Flasar, F.M. D/H Ratios on Saturn and Jupiter from Cassini CIRS. *Astron. J.* **2017**, *154*, 178. [CrossRef]

9. Lellouch, E.; Bézard, B.; Fouchet, T.; Feuchtgruber, H.; Encrenaz, T.; de Graauw, T. The deuterium abundance in Jupiter and Saturn from ISO-SWS observations. *Astron. Astrophys.* **2001**, *370*, 610–622. [CrossRef]

10. Melin, H.; Fletcher, L.N.; Irwin, P.G.J.; Edgington, S.G. Jupiter in the Ultraviolet: Acetylene and Ethane Abundances in the Stratosphere of Jupiter from Cassini Observations between 0.15 and 0.19 μm. *Astron. J.* **2020**, *159*, 291. [CrossRef]

11. Lellouch, E.; Feuchtgruber, H.; de Graauw, T.; Encrenaz, T.; Bézard, B.; Griffin, M. Deuterium and Oxygen in Giant Planets. In Proceedings of the The first ISO workshop on Analytical Spectroscopy, Madrid, Spain, 6–8 October 1997; Heras, A.M., Leech, K., Trams, N.R., Perry, M., Eds.; ESA Special Publication: Noordwijk, The Netherlands, 1997; Volume 419, p. 131.

12. Encrenaz, T.; Drossart, P.; Feuchtgruber, H.; Lellouch, E.; Bézard, B.; Fouchet, T.; Atreya, S. The atmospheric composition and structure of Jupiter and Saturn from ISO observations: A preliminary review. *Planet. Space Sci.* **1999**, *47*, 1225–1242. [CrossRef]

13. Sánchez-López, A.; López-Puertas, M.; García-Comas, M.; Funke, B.; Fouchet, T.; Snellen, I.A.G. The CH$_4$ abundance in Jupiter's upper atmosphere. *Astron. Astrophys.* **2022**, *662*, A91. [CrossRef]

14. Flasar, F.M.; Kunde, V.G.; Abbas, M.M.; Achterberg, R.K.; Ade, P.; Barucci, A.; Bézard, B.; Bjoraker, G.L.; Brasunas, J.C.; Calcutt, S.; et al. Exploring The Saturn System In The Thermal Infrared: The Composite Infrared Spectrometer. *Space Sci. Rev.* **2004**, *115*, 169–297. [CrossRef]

15. Noschese, R.; Cicchetti, A.; Sordini, R.; Cartacci, M.; Mura, A.; Brooks, S.; Lastri, M.; Filacchione, G.; Migliorini, A.; Moriconi, M.; et al. Juno/JIRAM: Planning and commanding activities. *Adv. Space Res.* **2020**, *65*, 598–615. [CrossRef]

16. Lacy, J.H.; Richter, M.J.; Greathouse, T.K.; Jaffe, D.T.; Zhu, Q. TEXES: A Sensitive High-Resolution Grating Spectrograph for the Mid-Infrared. *Publ. Astron. Soc. Pac.* **2002**, *114*, 153–168. [CrossRef]

17. Kessler, M. The Infrared Space Observatory (ISO) mission. *Adv. Space Res.* **2002**, *30*, 1957–1965. [CrossRef]

18. de Graauw, T.; Haser, L.; Beintema, D.; Roelfsema, P.; Agthoven, H.; Barl, L.; Bauer, O.; Bekenkamp, H.; Boonstra, A.J.; Boxhoorn, D.; et al. Observing with the ISO Short-Wavelength Spectrometer. *Astron. Astrophys.* **1996**, *315*, L49–L54.

19. Encrenaz, T.; de Graauw, T.; Schaeidt, S.; Lellouch, E.; Feuchtgruber, H.; Beintema, D.A.; Bezard, B.; Drossart, P.; Griffin, M.; Heras, A.; et al. First results of ISO-SWS observations of Jupiter. *Astron. Astrophys.* **1996**, *315*, L397–L400.

20. Roos-Serote, M.; Drossart, P.; Encrenaz, T.; Carlson, R.; Leader, F. Constraints on the Tropospheric Cloud Structure of Jupiter from Spectroscopy in the 5-μm Region: A Comparison between Voyager/IRIS, Galileo/NIMS, and ISO/SWS Spectra. *Icarus* **1999**, *137*, 315–340. [CrossRef]

21. Irwin, P.; Teanby, N.; Kok, R.; Fletcher, L.; Howett, C.; Tsang, C.; Wilson, C.; Calcutt, S.; Nixon, C.; Parrish, P. The NEMESIS planetary atmosphere radiative transfer and retrieval tool. *J. Quant. Spectrosc. Radiat. Transf.* **2008**, *109*, 1136–1150. [CrossRef]

22. Rodgers, C.D. *Inverse Methods for Atmospheric Sounding*; World Scientific: Singapore, 2000. [CrossRef]

23. Irwin, P.; Parrish, P.; Fouchet, T.; Calcutt, S.; Taylor, F.; Simon-Miller, A.; Nixon, C. Retrievals of jovian tropospheric phosphine from Cassini/CIRS. *Icarus* **2004**, *172*, 37–49. [CrossRef]

24. Fletcher, L.N.; Orton, G.S.; Sinclair, J.A.; Guerlet, S.; Read, P.L.; Antuñano, A.; Achterberg, R.K.; Flasar, F.M.; Irwin, P.G.J.; Bjoraker, G.L.; et al. A hexagon in Saturn's northern stratosphere surrounding the emerging summertime polar vortex. *Nat. Commun.* **2018**, *9*, 3564. [CrossRef]

25. Irwin, P.G.J.; Weir, A.L.; Smith, S.E.; Taylor, F.W.; Lambert, A.L.; Calcutt, S.B.; Cameron-Smith, P.J.; Carlson, R.W.; Baines, K.; Orton, G.S.; et al. Cloud structure and atmospheric composition of Jupiter retrieved from Galileo near-infrared mapping spectrometer real-time spectra. *J. Geophys. Res. Planets* **1998**, *103*, 23001–23022. [CrossRef]

26. West, R.A.; Baines, K.H.; Friedson, A.J.; Banfield, D.; Ragent, B.; Taylor, F.W. Jovian clouds and haze. In *Jupiter. The Planet, Satellites and Magnetosphere*; Bagenal, F., Dowling, T.E., McKinnon, W.B., Eds.; Cambridge University Press: Cambridge, UK, 2004; Volume 1, pp. 79–104.

27. Hale, G.M.; Querry, M.R. Optical Constants of Water in the 200-nm to 200-μm Wavelength Region. *Appl. Opt.* **1973**, *12*, 555–563. [CrossRef] [PubMed]

28. Martonchik, J.V.; Orton, G.S.; Appleby, J.F. Optical properties of NH3 ice from the far infrared to the near ultraviolet. *Appl. Opt.* **1984**, *23*, 541–547. [CrossRef] [PubMed]

29. Koukouli, M.; Irwin, P.; Taylor, F. Water vapor abundance in Venus' middle atmosphere from Pioneer Venus OIR and Venera 15 FTS measurements. *Icarus* **2005**, *173*, 84–99. [CrossRef]

30. Irwin, P.G.J.; Lellouch, E.; de Bergh, C.; Courtin, R.; Bézard, B.; Fletcher, L.N.; Orton, G.S.; Teanby, N.A.; Calcutt, S.B.; Tice, D.; et al. Line-by-line analysis of Neptune's near-IR spectrum observed with Gemini/NIFS and VLT/CRIRES. *Icarus* **2014**, *227*, 37–48. [CrossRef]

31. Lyons, J.R.; Gharib-Nezhad, E.; Ayres, T.R. A light carbon isotope composition for the Sun. *Nat. Commun.* **2018**, *9*, 908. [CrossRef]